Satellite-based surveys reveal substantial methane point-source emissions in major oil & gas basins of North America during 2022-2023

Fei Li[1, 2, 3], Shengxi Bai[1, 2, 3], Keer Lin[1, 2, 3], Chenxi Feng[4], Shiwei Sun[5], Shaohua Zhao[6], Zhongting Wang[6], Wei Zhou[6], Chunyan Zhou[6], and Yongguang Zhang[1, 2, 3]

[1]Jiangsu Center for Collaborative Innovation in Geographical Information Resource Development and Application, International Institute for Earth System Sciences, Nanjing University, Nanjing, China

[2]Jiangsu Provincial Key Laboratory of Geographic Information Science and Technology, Key Laboratory for Land Satellite Remote Sensing Applications of Ministry of Natural Resources, School of Geography and Ocean Science, Nanjing University, Nanjing, China

[3] Jiangsu International Joint Carbon Neutrality Laboratory, Nanjing University, Nanjing, China

[4] School of Atmospheric Sciences, Nanjing University, Nanjing, China

[5] Key Laboratory of Transportation Meteorology of China Meteorological Administration, Nanjing Joint Institute for Atmospheric Sciences, Nanjing, China

[6] Ministry of Ecology and Environment Center for Satellite Application on Ecology and Environment/ State Environmental Protection Key Laboratory of Satellite Remote Sensing, Beijing, China

Corresponding author: Yongguang Zhang (yongguang_zhang@nju.edu.cn)

28 February, 2024

This is a non-peer reviewed preprint submitted to EarthArXiv, submitted to peer review at Journal of Geophysical Research: Atmospheres.

Key Points:

- The new Chinese Gaofen5-01A/02 hyperspectral satellite missions have great capability in methane mapping.
- We find a substantial methane point-source emissions in Permian Delaware Tight US after COVID-19 during 2022-2023.
- Satellite-based survey can effectively improve bottom-up regional methane emissions inventories.

Plain Language Summary

Reducing methane (CH_4) leaks from Oil & Gas (O&G) production is crucial for abating climate change. However, detecting these abnormal CH_4 emissions globally is challenging as they often occur unexpectedly. Satellite remote sensing with hyperspectral imaging spectrometer provides a novel approach for top-down monitoring. These instruments produce CH_4 plume maps, enabling the quantification of emissions. In this research, we conduct a comprehensive survey in major O&G basins of North America during 2022-2023 using the new Chinese Gaofen5-01A/02 satellite. Through repeated observations by high-resolution satellites, we capture CH_4 emission dynamics in sample basins and quantify their contribution to regional methane budget. Our results demonstrate the value of high-resolution satellite observations in reducing uncertainties in quantifying anthropogenic CH_4 emission and supporting strategies for emission mitigation.

Abstract

Utilizing imaging spectroscopy technology to identify methane super-emitters plays a vital role in mitigating methane emissions in the Oil & Gas (O&G) sector. While earlier research has uncovered significant point-source methane emissions from O&G production in the US and Canada, which are key regions with large methane emissions, a comprehensive post-COVID-19 survey has been notably absent. Here, we perform a detailed survey of methane super-emitters across multiple basins of North America (Marcellus Shale US, Haynesville/Bossier Shale US, Permian Delaware Tight US and Montney Play Canada) using the new Chinese Gaofen5-01A/02 (GF5-01A/02) satellite measurements during 2022-2023. We detect 48 extreme methane point-source emissions with flux rates of 646 to 16071 kg h^{-1}. These emissions exhibit a highly skewed and heavy-tailed distribution, constituting approximately 30% of the total flux in sample region, with a range of 13% to 63%. Moreover, we observe a 66.7% reduction in methane emissions in Permian Delaware Tight region during COVID-19, followed by fluctuations until spring 2022. By summer 2023, methane emissions rebound to previous magnitude (0.66 ± 0.20 Tg a^{-1}). Using these point-source surveys, we further quantify a regional methane emission of 1.08 ± 0.02 Tg a^{-1} in Delaware subbasin. This estimation closely aligns with top-down inversions (0.86 ± 0.03 Tg a^{-1}) from TROPOMI. The upscale estimation underscores the effectiveness of high-resolution remote sensing measurements in improving bottom-up emissions inventories and refining regional methane emission assessments. Our results highlight the potential climate benefits derived from regular monitoring and specific remediation efforts focused on relatively few strong point-source emissions.

1 Introduction

Prompt detection of abnormal methane (CH_4) emissions in Oil & Gas (O&G) field, coal mine and liquefied natural gas terminal would enable action for climate change mitigation. CH_4 emissions from O&G facilities predominantly emanate from key infrastructures, including wellheads, compressor stations, tank batteries, pipelines and flares (Lyon et al. 2016), forming easily recognizable "point-source emissions". Numerous studies indicate that CH_4 emissions from O&G facilities exhibit a heavy-tailed distribution with a small number of large point sources contributing significantly to total emissions (e.g., Brandt et al. 2014; Cusworth et al. 2021; Duren et al. 2019). This disproportionate contribution often stems from malfunctions and abnormal operating conditions, such as fugitive emissions from leakage, venting, and facility blowouts (Lyon et al. 2021; Rutherford et al. 2021; Zavala-Araiza et al. 2021). Detecting these unexpected emissions of relatively small sizes globally poses a significant challenge (Cusworth et al. 2021). Additionally, the duration, quantity, and frequency of these leaks have large variations in different regions and periods (Irakulis-Loitxate et al. 2021; 2022b).

Spaceborne imaging spectroscopy offer a unique observational approach for mapping CH_4 point-sources emissions. These instruments, utilizing the radiance in the SWIR range, can discern subtle signal changes from methane absorption (Frankenberg et al. 2005; Jacob et al. 2016; Jacob et al. 2022). Recent advancements in hyperspectral satellites have demonstrated their potential to map and quantify point-source methane emissions. Hyperspectral imaging spectrometers, with ~10 nm spectral resolution and 30~60 m spatial resolution, such as those onboard the PRISMA (PRecursore IperSpettrale della Missione Applicativa) (Guanter et al. 2021), EnMAP (Environmental Mapping and Analysis Program) (Roger et al. 2024), EMIT (Earth Surface Mineral Dust Source Investigation) (Thorpe et al. 2023a), GF5-01-AHSI

(Gaofen5-01) and ZY1-02D-AHSI (Ziyuan-1 02D) (Liu et al. 2019), exhibit significant ability for mapping CH_4 point-sources in O&G basins and coal mining areas. The recently operational GF5-01A/02 missions, launched on 7 Sep.2021 and 9 Dec. 2022 respectively, offer an opportunity to enhance our ability to quantify methane point-source emissions. However, the capabilities of these latest missions for methane mapping remain unclear in comparison to the high performance of the first-generation AHSI on board China GF5 (GF5-01-AHSI) in detecting methane point-source emissions.

As the largest O&G producer globally, the US contributes 15% of the global O&G CH_4 emissions for 2019 (8.1 Tg a^{-1}) (Scarpelli et al. 2022), making it a major methane emitter in the O&G industry. The Permian Basin with the largest oil production in the US, responsible for over 40% of the country's oil and gas production (FRBD, 2022), has garnered increased attention for estimations of methane emissions. Despite previous studies utilizing satellite imaging spectroscopy for high-resolution surveys of methane point emitters in individual O&G basins, these have mainly focused on a few observations (Esparza et al. 2023; Irakulis-Loitxate et al. 2021). However, considering the impact of the COVID-19 pandemic on CH_4 emissions (Thorpe et al. 2023b), it remains unclear if the observed temporary reductions extend across the entire O&G supply chain, all basins, and sectors. Further surveying efforts are needed to address this uncertainty.

In this work, we aim to evaluate the impact of the COVID-19 pandemic on methane emissions in various North American O&G basins (Marcellus Shale US, Haynesville/Bossier Shale US, Permian Delaware Tight US, and Montney Play Canada) from 2022 to 2023. Employing GF5-01A/02, we identify CH_4 point sources, quantify emission flux, and attribute contributions to specific facilities in these regions. Additionally, we estimate regional methane budgets exclusively using point source observations in Permian Delaware Tight US and compare them to regional methane flux inversions based on TROPOMI/GOSAT XCH_4. Through this comprehensive approach, we aim to discern the contribution of these significant point sources to the regional methane budget. Ultimately, we leverage satellite observations to enhance bottom-up inventories and highlight opportunities for emission reduction.

2 Material and Methods

2.1 Satellite imaging spectroscopy data

The GF5-01A/02 satellites are the 2nd generation satellites of the Gaofen-5 series (Chinese civilian remote sensing satellites) and were launched on 7 Sep.2021 and 9 Dec.2022, respectively. They have been operation over two years with a large number of global observations to date. GF5 satellite is configured with six types of payloads including hyperspectral and directional polarization instruments, designed for environmental monitoring, encompassing aerosol, cloud and greenhouse gas monitoring (Chen et al. 2022). The Advanced Hyperspectral Imager (AHSI) aboard the GF5 is a groundbreaking spaceborne hyperspectral camera. It employs both an improved three-concentric-mirror (Offner) configuration and a convex-grating spectrophotometry. Covering a spectral window from 400 to 2500 nm, the AHSI achieves a spatial resolution of 30 m with a swath of 60 km. It comprises 330 spectral bands with 5 and 10 nm spectral resolution in the VNIR and SWIR, respectively (Liu et al. 2019). The distinctive features of wide coverage, fine spatial resolution, high signal-to-noise ratio (SNR) (500 in the SWIR bands), and excellent spectral uniformity set GF5-01A/02 apart from other hyperspectral imaging spectrometers. These characteristics provide significant advantages in mapping point-source CH_4 emissions (Irakulis-Loitxate et al. 2021). In addition to the GF5-01A/02, NASA's EMIT, launched on 14 July 2022, and is operational on the International Space Station. EMIT have 285 distinct wavelengths at a spectral resolution of 7.4 nm, ranging from 381 to 2493 nm. It achieves 60 m spatial resolution, an 80 km swath, and a SNR from 500 to 750 in most bands. This makes EMIT also well suited for identifying methane super-emitters (Thorpe et al. 2023a). More details of these satellites can be seen in Table 1.

In this work, we integrated a set of 27 images obtained from GF5-01A/02 and EMIT to cover major O&G basins in North America. The acquisitions employed in this study predominantly spanned from February 2022 to September 2023. We use L1 level datasets from 3 scenes of GF5-01A, 20 scenes of GF5-02 and 4 scenes of EMIT, with the EMIT scenes serving as supplementary data (see Table A1).

2.2 Principles in the retrievals of methane column concentration enhancement

Methane column concentration enhancement (ΔX_{CH4}) can be retrieved through the application of the Matched Filter (MF) method. It characterizes the background radiance as a multivariate Gaussian with mean (μ) and covariance ($\sum$), under the assumption that each input radiance is expressed as the average radiance plus the perturbation resulting from a variation in methane column concentration (Thompson et al. 2016):

$$x = \mu + \Delta X_{CH4} \cdot t \tag{1}$$

where x represents the radiance spectrum at sensor, and t is the target signature, defining the radiance spectrum equivalent to the absorption of one unit of methane concentration in relation to background. t is derived from the product of the unit methane absorption (k) spectrum and the background mean. k is calculated from a Look-Up Table linking CH_4 transmittance spectra, obtained from the HITRAN database, to methane concentration (Gordon et al. 2017). Figure 1a shows an illustrative example of a k target unit absorption spectrum. By maximizing the likelihood of Eq.1 (Eismann 2012), ΔX_{CH4} can be described as follows:

$$\Delta X_{CH4} = \frac{(x-t)^T \sum^{-1} t}{t^T \sum^{-1} t} \tag{2}$$

The application of the MF to the strong CH4 absorption bands at 2300 nm is a widely adopted approach (Dennison et al. 2013; Foote et al. 2020; Thompson et al. 2015). Hence, we apply the MF technique for the strong CH_4 absorption bands within the 2100-2450 nm. Despite the 1700 nm absorption bands generally exhibiting higher radiance levels, the CH_4 absorption is significantly weaker (see Figure 1 (b) and (c)), leading to more noise in methane retrievals.

2.3 Methane plume detection and quantifications

The identification of CH_4 plumes initiates with a visual examination of the ΔX_{CH4} maps obtained. Distinguishing the plumes from the background is usually straightforward in maps with minimal random noise, thanks to the distinctive shape of the plumes. After the initial identification of plumes, their shape is cross-verified with the GEOS-FP 10 m wind direction data to ensure consistency. Once confirmed, the plumes are matched with high-resolution images to precisely locate the infrastructure responsible for the emissions.

The subsequent step in the detection process focuses on each identified plume, separating it from the surrounding background to calculate the whole emission area. Here, a semiautomated approach is employed. The plume is segregated using a mask set at a 95% confidence level and further refined with a square dilation mask spanning multiple pixels. Like the median filter method, this dilation mask guarantees the inclusion of the plume tails in the identified area. This method not only minimizes discontinuities arising from the spatial pattern of a CH_4 plume but also ensures a more cohesive selection of the plume. Lastly, feature selection techniques are employed to eliminate any detected outliers in close proximity to the plumes (Szeliski, 2022).

After identifying the CH_4 plumes, we use the integrated mass enhancement (IME) method to quantify the flux rate for each methane plume (Frankenberg et al. 2016; Varon et al. 2018). The IME is calculated in *kg* units, representing the overall excess mass of CH_4 present in the plume:

$$IME = k \sum_{i=1}^{n_p} \hat{\alpha}(i) \tag{3}$$

where k is a scaling factor (5.155×10^{-3} *kg/ppb*), and n_p is the number of pixels within the plume The scaling factor k transforms the sum of pixel-wise CH_4 concentration in *ppb* to *kg*, considering Avogadro‘s law, the molecular weight of CH_4 and the 30-m pixel size. Q is derived as follows:

$$Q = \frac{U_{eff} \cdot IME}{L} \tag{4}$$

where L is the plume length scale determined as $L = \sqrt{A}$. A is the square root of the area of the detectable plume. U_{eff}=f(U_{10}) is an effective wind speed. The U_{eff} term is computed from the local 10-m wind speed (U_{10}) in Eq. 5 (Li et al. 2023):

$$U_{eff} = 0.38 \cdot U_{10} + 0.41 \tag{5}$$

This linear relationship is from the large-eddy simulations (LES) that are specifically tailored for the spatial resolution and ΔX_{CH4} retrieval precision similar to satellite data. A linear model is found to provide the best fit (Varon et al., 2018, Cusworth et al. 2019). U_{10} data are extracted from the GEOS-FP dataset.

The accuracy of satellite-based methane point-source emissions detection and quantification has been validated against a few controlled CH_4 release experiments (Sherwin et al. 2023a; Sherwin et al. 2023b). Quantification error across all satellites and participants are generally low. In the case of all identified emissions using hyperspectral instruments, the parity lines for each satellite team consistently align closely with the ideal 1:1 line. The accuracy of mean estimates for all combinations of satellite teams exceeds 80%, and the R^2 values for linear fits for fully blinded estimates range from 0.89 to 0.97. These validations demonstrate the good performance of MF method in identifying and measuring methane point-source emissions.

2.4 Methane point sources attribution

The abundant spatial detail provided by high resolution satellite data facilitates the detection of CH_4 point sources, including those within O&G extraction facilities, and tank batteries or compressor stations. We leverage high spatial resolution satellite images from platforms like Google Earth, Esri Map, and Bing Maps, co-registered with ΔX_{CH4} maps, to assign point sources to specific facilities. In instances where high-resolution imagery data are unavailable for the detected methane plume's time and location, Sentinel-2A/2B images are utilized as a substitute.

We have gathered specific details about O&G extraction platforms in the interactive PermianMAP provided by the Environmental Defense Fund. Others not available in PermianMAP have been obtained through Global Energy Monitor and visual interpretation of Sentinel-2A/2B historical images. With this information, we can pinpoint the emission facilities associated with the detected plumes.

2.5 Estimation of integrated emission rate and regional methane budget

Our plume detections capture specific moments when emissions exceed 500 kg h^{-1} during satellite overpasses, providing snapshots in time. To facilitate a meaningful comparison, we convert emissions from per-hour to per-year units (Irakulis-Loitxate et al., 2021). Recognizing the intermittent nature of most point-source emissions, we make the assumption that the leakage facility emits consistently throughout the entire event with a relatively constant flux (Irakulis-Loitxate et al. 2022a). The detected point-sources serve as a representative ground sample of significant emitters on the regional scale, allowing us to scale up and generate a comprehensive annual estimation of CH_4 emissions.

Moreover, we derive the regional methane emissions based on point-source observations in Permian Delaware Tight US. This estimation involves employing Kriging interpolation with a spherical semi-variogram model, using a maximum radius setting of 12 β values. Considering that the interpolation results can be influenced by the grid size and spatial density of point sources, and to prevent overfitting while minimizing interpolation errors, we adopt a 0.3125° × 0.3125° grid sample unit to encompass the entire Delaware subbasin. This choice closely aligns with the spatial resolution of atmospheric inversion results.

Additionally, we have conducted a comparison between the individual point-source emissions we identified and the area-integrated emission estimates derived from both the bottom-up emission inventory of GFEI v2/EPA v2 (Maasakkers et al., 2023; Scarpelli et al., 2022) and the top-down inversions of TROPOMI/GOSAT (Lu et al., 2023; Shen et al., 2022). It should be noted that such comparison between single-point and area-integrated CH_4 emissions is solely intended to offer additional context on the level of the extreme CH_4 point-source emissions. Details of the emission inventory and inversion estimates are provided in Table 2.

3 Results

3.1 Characteristic of observed methane point-source emissions

Utilizing the methodologies outlined earlier, we perform a high-resolution survey of all detectable CH_4 point-source emissions across major O&G basins in North America. This survey incorporates all accessible imagery captured by GF5-01A/02 & EMIT from Feb.2022 to Sep.2023. In total, we identify 48 extreme point sources, and their spatial distribution along with emission magnitudes are illustrated in Figure 2. The majority, specifically 40, are located in Permian Delaware Tight US, while the remaining point source emissions are relatively dispersed across other basins, including Montney Play Canada (4 plumes), Marcellus Shale US (2 plumes), and Haynesville/Bossier Shale US (2 plumes). Of the 48 methane plumes observed during this survey, the average emission is 3,575 ± 1,249 kg h^{-1} and the total emission is 171,617 ± 59,937 kg h^{-1}. Furthermore, out of the detected 48 plumes, 35 are identified by the GF5-01A/02 satellites, showcasing outstanding performance of the GF5 series satellite in detecting extreme methane point-source emissions.

Figure 3 shows some examples of individual methane plumes observed using GF5-01A/02 instruments across multiple basins and various facilities (Fig. S1 and Table S2 for comprehensive details of all emission locations, flux rates and type of facility). The emissions exhibit considerable variability in both source types and flux rates. For instance, plume A represents a substantial emission with high flux rates (Q = 6,452±2,422 kg h^{-1}) from a malfunctioning flare, while plume Q corresponds to a source emission (Q =3,392±967 kg h^{-1}) attributed to incomplete combustion of a flare in a well pad. Additionally, plume T (Q =1,844±464 kg h^{-1}) and plume V (Q = 1,313±436 kg h^{-1}) are associated with leakage from a tank battery. It is important to note that our plume detections capture snapshots of emissions with flux rates exceeding 500 kg h^{-1} when satellite overpass. Most emission sources detected align serendipitously with the space-borne missions (Fig. S1). More comprehensive statistics for these basins will emerge as additional data is analyzed, allowing for targeted assessments during subsequent missions.

We further analyze the characteristic of flux rates stemming from identified point source emissions (Figure 4). The emissions from these point sources exhibit a markedly skewed distribution, typically falling within the range of 500 to 4,000 kg h^{-1}. As displayed in the inset plot of Figure 4, relatively substantial extreme point emitters are detected (>1,000 kg h^{-1}) that account for more than 78% of the whole CH_4 emission rates in each survey. Combining all surveys, it is noteworthy that a mere 8.33% of emitters contributed to over 30% of the whole emissions detected in the studied region, with the largest plume notably contributing 9.36% of the total methane detected.

Figure 5 illustrates the comparisons of methane point source emissions from our study during 2022 and 2023 with previous surveys. The observed emission intensities in this study (ranging from 646 to 16,071 kg h^{-1}) exceed the median values (299 kg h^{-1}) in comprehensive regional airborne surveys of the US from 2019 to 2021 (Cusworth et al. 2022), exceeding earlier airborne survey findings as well (Duren et al. 2019). In addition, our study identifies a higher number of methane extreme emitters compared to US airborne surveys, at a median emission flux rate of 2,050 kg h^{-1}. Our results also indicate higher emission intensities compared to a previous satellite survey in the Permian region from 2019 to 2020 (median of 1,850 kg h^{-1}) (Irakulis-Loitxate et al., 2021), potentially suggesting a rebound in methane emissions after COVID-19. This comparison contextualizes the emission magnitudes of identified super CH_4 emitters, affirming that our surveys align with that observed from field campaigns.

We also examine the cumulative distribution of methane point-source emissions during 2022 and 2023, comparing them with previous studies in the Permian basin (Figure 6). The smallest emission rate identified during 2022 and 2023 is 646 kg h^{-1} (Figure 6), with emissions exceeding this threshold contributing to 22% of the total CH_4 emissions from airborne surveys in the Permian Basin (Cusworth et al., 2022). The coarser spatial resolution of spaceborne instruments makes them less sensitive to low CH_4 emissions, making them to capture a large number of CH_4 emissions significantly larger than those observed in airborne surveys. Consequently, the distribution of spaceborne observations skews towards larger emissions with respect to airborne surveys (e.g., AVIRIS-NG and GAO) conducted in multiple US regions. Notably, the cumulative distribution of emission rates during 2022-2023 is also shifted towards larger emissions compared to spaceborne surveys in 2019-2020 (Irakulis-Loitxate et al. 2021).

This finding reaffirms the substantial CH_4 emissions in the Permian Basin after the COVID-19 period.

In addition, we assess the contribution of emissions from these super emitters on the regional methane budget (Figure 7), by comparing to both bottom-up inventories (US EPA inventory) and top-down inversions (Lu et al. 2023; Maasakkers et al. 2023; Shen et al. 2022). Our findings indicate that these super emitters contribute an average of 30% to each basin's total emissions with a range of 13% to 63% across all basins and time periods. Notably, we attribute 63% of the regional emissions to point sources in Permian Delaware Tight US. Furthermore, the bottom-up inventory tends to underestimate the overall CH4 flux compared to estimates derived from GOSAT or TROPOMI, aligning with previous findings from top-down analyses (Alvarez et al. 2018).

3.2 Estimation of regional methane budgets from point sources observations

We quantify regional methane budgets by integrating point-source observations and spatial interpolation in the methane-intensive Permian Delaware Tight US. In Figure 8, our regional estimation is compared with (1) total methane fluxes obtained from a top-down inversion from TROPOMI XCH_4 (Shen et al. 2022) and (2) bottom-up emission inventories for O&G sectors (US EPA inventory) (Maasakkers et al. 2023). TROPOMI XCH_4 measurements indicate significant methane enhancements, reaching ~30 ppb above the background, over the Delaware basin from February 2022 to October 2023 (Figure 8a). The spatial distribution of methane emission from atmospheric inversion (Shen et al. 2022) reveals a single-branch distribution over the Delaware basin, corresponding to the major O&G production region (Figure 8b). As can be seen in the regional-scale methane enhancements and methane emissions generated from TROPOMI observations and inversion estimate (Figure 8a and b), the regions exhibiting the highest density of super emitters in our satellite-based survey align with the most substantial methane enhancements and the highest methane fluxes over the central and eastern regions of Delaware subbasin.

Regarding the regional methane budget, we estimate methane emissions at 1.08±0.02 Tg a^{-1} in the Delaware basin during 2022 and 2023. Notably, our regional estimation solely based on point-source observations closely aligns with top-down atmospheric inversions (0.86±0.03 Tg a-1) from TROPOMI, even though the time periods differ (refer to Figure 8b and c). The spatial distribution of methane emissions demonstrates remarkable consistency between our spatial interpolation and atmospheric inversions, emphasizing that the emissions predominantly originate from significant point-source emitters in the Delaware subbasin. In contrast, the EPA greenhouse gas inventory significantly underestimates the total methane flux for the Delaware subbasin (Figure 8d), providing a mere estimation of 0.18 Tg a^{-1}. The inventory generally falls short of the total CH_4 emissions inverted from GOSAT or TROPOMI, as shown in previous top-down analyses (Alvarez et al. 2018). These comparisons underscore the effectiveness of upscaling estimations from high-resolution satellite data in overcoming regional inversion uncertainties. These findings also highlight the importance of satellite point-source observations in the estimation of regional methane emission, providing an additional bottom-up approach to mitigate the underestimation inherent in bottom-up inventories.

3.3 Temporal evolution of methane point source emissions

Utilizing multi-period satellite surveys enables us to examine the temporal trends of methane point-source emissions in these O&G basins during 2022 and 2023. In Figure 9(a), methane emission rates and the number of detected point sources are presented based on multi-month space-borne surveys. From February 2022 to October 2023, variations in the number of observed point sources are evident, reaching a maximum of 10 plumes in a single day. Correspondingly, point-source aggregated emissions range between 0.013 Tg a^{-1} and 0.583 Tg a^{-1}. Notably, we observe that the number of detected point sources does not consistently correlate with the magnitude of methane emissions. A few super-emitters can significantly contribute to the overall leak volume.

We then compare methane emission rates in the Permian Delaware Tight US for different time period. In Figure 9 (b), emissions from various airborne/spaceborne surveys in the Delaware subbasin are compared before and after COVID-19. Notably, point-source CH_4 emissions in fall 2019 are significantly higher (0.84 ± 0.27 Tg a^{-1}) than that in subsequent surveys from winter 2020 to spring 2022 (ranging from 0.24 ± 0.11 Tg a^{-1} to 0.52 ± 0.15 Tg a^{-1}) during the COVID-19 period. However, methane emissions in summer 2023 rebound to levels similar to fall 2019. The sharp decline in emissions after fall 2019 may be attributed to factors such as the impact of COVID-19 and changes in the oil market, leading to decreased flaring activities and well completions. Additionally, the diverse characteristics of operators and supply chain activities in Permian contribute to high variability in emissions, as observed in aggregated airborne point-source emissions during fall 2019 (Cusworth et al. 2021). Therefore, a more comprehensive and extended analysis is required to distinguish long-term trends from the changes of point-sources CH_4 emission in the Permian Delaware Tight US.

3.4 Attribution of emission sources

The high spatial resolution of remote sensing data enables us to precisely associate the identified point sources with specific infrastructure. We categorize emissions based on the emission source (tank battery, compressor station, flaring, wellhead and unknown) and the sector of the emitting infrastructure (O&G, coal mining, electricity generation, livestock and solid waste). A breakdown of the characteristics of the emitting infrastructure detected by spaceborne instruments is presented in Figure 10 (a) (see Table A1 for more details), and emission sectors with point source characteristics detected by airborne instruments is displayed in Figure 10 (b). Whether viewed from emission sources in spaceborne surveys or emission sectors in airborne surveys, we observe a surprisingly high proportion of CH_4 emissions from the O&G sector, ranging from 87% to 98%. In comparison to a previous Permian survey (Irakulis-Loitxate et al. 2021), the proportion of methane leaks from wellheads and tank batteries has increased, while the proportion from compressor stations and flaring has decreased. Our source analysis indicates that wellheads have become significant emitters (22.9%) during the post-COVID-19 survey, potentially due to recently developed wells, associated infrastructures, and increased productivity. Furthermore, the flux rates of detected emissions from wellheads, tank batteries, and compressor stations range from 646 to 14,156 kg h^{-1} (refer to table S1). This range encompasses our entire emission distribution (Fig. 4), with high emissions exceeding 4,000 kg h^{-1} possibly resulting from accidents or malfunctioning equipment. These findings are useful to help mitigate the design and regulation of O&G production activities in North America.

4 Discussion

4.1 Methane point-source emissions monitoring

In this study, we utilize spaceborne imaging spectroscopy data to perform a survey of individual methane super emitters in North America, a prominent global methane hotspot, spanning the years 2022 to 2023 after COVID-19. Most detected plumes are located in Permian Delaware Tight US, the rest of plumes are relatively dispersed across other basins. This distribution aligns with the regions of highest CH_4 emission identified in top-down inversions by Shen et al. (2022) but shows less correlation with the bottom-up inventory from the updated Global Fuel Exploitation Inventory (GFEI-v2) (Scarpelli et al. 2022) (Fig. A2). Methane emissions observed by GF5-01A/02-AHSI and EMIT from individual plumes range from 646 to 16,071 kg h^{-1}, closely aligning with previous findings in the Permian region (522~18,492 kg h^{-1}) (Irakulis-Loitxate et al. 2021). Methane emissions exceeding 646 kg h^{-1} contribute to 22% of the total emissions measured in US airborne surveys (Cusworth et al. 2022), underscoring the potential of the recently launched GF5-01A/02-AHSI to map large regions inaccessible to airborne surveys. Notably, some emissions detected by GF5-01A/02-AHSI fall below minimum detection thresholds determined in other studies utilizing multispectral satellite data (Ehret et al. 2022; Irakulis-Loitxate et al. 2022a; Pandey et al. 2023; Varon et al. 2021), highlighting the significance of these advanced technologies in detecting emissions that may be missed in surveys relying solely on publicly available remote sensing datasets.

In comparison to prior surveys in North America (Cusworth et al. 2022; Irakulis-Loitxate et al. 2021), the methane point-source emissions identified in this study show a shift toward larger emissions, with a higher median CH_4 emission flux of 2050 kg h^{-1} (refer to Figure 5 and Figure 6). This shift indicates an increase in methane emissions in North America following the COVID-19 period, possibly influenced by the resurgence of O&G prices and production in the post-COVID-19 period (Thorpe et al. 2023b). These findings suggest that the average emission rate per source has indeed risen, and the production activity have recovered following the COVID-19 pandemic.

Furthermore, the pronounced heavy-tailed emission distribution observed in this study underscores the significant contribution of a few "super-emitters" to the overall methane emissions, consistent with prior research in the US O&G sector (Cusworth et al. 2021; Frankenberg et al. 2016; Irakulis-Loitxate et al. 2021; Yu et al. 2022). It is anticipated that as ongoing monitoring in North America continues, the emission distribution will progressively exhibit a heavier tail with more sample size, capturing more super emission events. Consequently, this implies that a substantial portion of the detected methane emissions from these basins could be alleviated by promptly addressing a small number of leaks (Mayfield et al. 2017). With 30% of regional methane emissions detected over these basins originating from these super-emitters, rapid detection and repair of these significant CH_4 leaks could significantly reduce the environmental impact with less additional labor.

4.2 Implications for estimation of regional methane budget from satellite-based point-source observations

In Permian Delaware Tight US, our upscaling estimate based on extrapolation of limited satellite-detected methane emissions (1.08 ± 0.02 Tg a^{-1}) closely align with the atmospheric inversion results with TROPOMI observations (0.86 ± 0.03 Tg a^{-1}) (Figure 8). However, there are more than four times lower in the EPA inventory data (0.18 Tg a^{-1}). Our results indicate that current bottom-up inventories for national CH_4 emissions in the United States underestimate real emissions, highlighting the potential of high spatial resolution remote sensing measurements to offer a more accurate representation. Our results affirm that remote sensing technologies, such as hyperspectral satellite, can significantly enhance bottom-up emissions inventories, refine regional methane emission estimation, and mitigate uncertainties.

Prior research proposes potential explanations for the disparity between bottom-up and top-down methane emission estimation. One factor is the oversight of unexpected leaks or point source emitters in inventories (Alvarez et al. 2018), with these super-emitters being recognized contributors to total methane emissions as shown in this study. Another contributing factor is the utilization of outdated emission factors in inventories, and updating these factors has proven effective in minimizing the divergence (Rutherford et al. 2021). However, emission factors can vary across regions, and those from a single region may not be used in other regions or countries (Rutherford et al. 2021). Spatiotemporal misalignment is another potential reason for discrepancies (Vaughn et al. 2018), as the timing of measurements have important impact on the accuracy due to the variable nature of methane emissions over time. It is crucial to point out the uncertainties in top-down inversions, which may overestimate actual emissions. Combining inventory data with satellite-based surveys as shown in this study is essential to mitigate these uncertainties and inconsistencies.

4.3 Monitoring the temporal evolution of point-sources CH_4 emissions

A prior study indicates a continuous rise in O&G production until the COVID−19 pandemic (e.g., Lyon et al., 2021). Consequently, methane emissions reached their peak by fall 2019 (0.84 ± 0.27 Tg a^{-1}). During the pandemic, methane emissions experienced a significant decline, followed by fluctuations from winter 2020 to spring 2022 (from 0.24 ± 0.11 Tg a^{-1} to 0.52 ± 0.15 Tg a^{-1}). Upon entering the post-COVID-19 period in 2023, methane emissions rebounded alongside increased O&G prices and production (0.66 ± 0.20 Tg a^{-1} in the summer of 2023). These findings underscore the capability of hyperspectral imaging spectroscopy to capture variations in methane emissions associated with long-term trends such as the epidemic. This highlights the significant potential of remote sensing measurements to quantify methane emissions and depict temporal trends, thereby enhancing our comprehension of regional methane budgets. Considering the substantial rise in global atmospheric CH_4 growth rates post-2020 (Tollefson 2022), there is an urgent demand for methane mitigation facilitated by using satellite imaging spectroscopy techniques.

4.4 Limitations and outlook

The GF5-01A/02-AHSI missions contribute significantly by offering extensive coverage and fine spatial resolution, paving the way for potential identification of fugitive emissions. This study presents the initial instances of GF5-01A/02-AHSI imaging spectrometer observations capturing methane emissions from the O&G sector across North America. Additionally, we showcase the instrument's capability to map and quantify various emission sources, attributing them to specific facilities. These capabilities, driven by the 30 m spatial resolution and 60 km swath, are crucial for accurately assessing regional methane budgets (Jacob et al. 2022). Nevertheless, this study offers only a two-year snapshot of multi-basin methane emissions, with the initial GF5-01A/02-AHSI observations lacking complete spatial coverage and repeat mapping essential for assessing persistence. Despite these limitations, the preliminary findings from the spaceborne survey reveal significant regional variability in methane emissions, shedding light on areas with substantial emissions and incomplete activity reporting.

Future studies combining measurements from various airborne/spaceborne instruments can enhance global coverage and revisit frequency (Chulakadabba et al. 2023; Pandey et al. 2023), a critical step in determining emission persistence and reducing uncertainty in the regional to global CH_4 budget (Mayfield et al. 2017). More specifically, a number of high-resolution and hyperspectral satellite missions currently in orbit (i.e., Chinese ZY1-02D/02E satellites, Italian PRISMA satellite, German EnMAP mission and Canadian GHGSat constellation) and upcoming spaceborne imaging spectroscopy missions (i.e., Carbon Mapper, CHIME and SBG missions) will contribute to a comprehensive scenario for point-source methane mapping. In addition, daily observations from TROPOMI and the soon-to-be-launched MethaneSAT mission, along with long time-series observations from multispectral systems (GF5-01/02-VIMS, Sentinel-2/3, Landsat-8/9, WorldView-3) can be served as complementary data. As we approach the Paris target, the collaborative utilization of these missions holds the promise of a breakthrough in mitigating unintended methane leakages from the Oil & Gas industry in the coming years and has significant implications for measuring global methane pledges.

5 Conclusions

In this work, we demonstrate the potential of Chinese new hyperspectral satellites (GF5-01A/02-AHSI) in detecting and quantifying methane point-source emissions across multiple North American basins from 2022 to 2023. The identification of 48 methane super-emitters, with flux rates between 646 and 16071 kg h^{-1}, reveals a skewed and heavy-tailed emission distribution from O&G infrastructures. Specifically, the wellhead emerges as a major emitter (22.9%) post-COVID-19. Regional methane estimation indicates that point sources contribute approximately 30% of the total methane flux (13 to 63% range). In Permian Delaware Tight US, methane emissions decline by 66.7% after COVID-19, then rebound to previous levels by summer 2030 (0.66 ± 0.20 Tg a−1). Our upscaling estimates (1.08 ± 0.02 Tg a^{-1}) from point-source observations closely align with atmospheric inversion results (0.86 ± 0.03 Tg a^{-1}). The findings underscore the value of hyperspectral imaging spectroscopy in enhancing bottom-up inventories, refining regional methane estimates, and reducing uncertainties. Integrating bottom-up data with satellite data holds the potential to provide a better understanding of methane emissions, thereby enabling targeted CH_4 emission mitigation strategies to reduce their impact on climate change.

Open Data Sources

All data underpinning this publication are openly available.

GF5-01A/02-AHSI L1 data are available here: https://data.cresda.cn/.

EMIT L1B data are available here: https://search.earthdata.nasa.gov/search.

Updated global fuel exploitation inventory (GFEI v2) are available here: https://doi.org/10.7910/DVN/HH4EUM.

EPA greenhouse gas inventory (EPA v2) are available here: https://www.epa.gov/ghgemissions/us-gridded-methane-emissions.

Top-down flux inversion with GOSAT observations is available here: https://github.com/luxiaoatchemsysu/Data-USoilgasCH4.

Top-down flux inversion with TROPOMI observations is available here: https://doi.org/10.18170/DVN/JPKFU6.

Sentinel-2A/2B data are available here: https://dataspace.copernicus.eu/.

Global Oil & Gas (O&G) infrastructure database are available here: https://globalenergymonitor.org/.

GEOS-FP data are available here: https://portal.nccs.nasa.gov/datashare/gmao/geos-fp/das/.

Acknowledgement

This work is supported by the project of National Key Research and Development Program of China (2022YFE0209100). We would like to thank the China Center for Resources Satellite Data and Application for the GF5 series data. Thanks are also extended to the NASA's Jet Propulsion Laboratory for sharing the EMIT data used in this study. These valuable contributions significantly enriched the data resources and supported the successful execution of this research project.

References

Alvarez, R. A., et al. (2018), Assessment of methane emissions from the U.S. oil and gas supply chain, *Science*, *361*(6398), 186-188, doi:10.1126/science.aar7204.

Brandt, A. R., et al. (2014), Methane Leaks from North American Natural Gas Systems, *Science*, *343*(6172), 733-735, doi:10.1126/science.1247045.

Chen, L., et al. (2022), An Introduction to the Chinese High-Resolution Earth Observation System: Gaofen-1~7 Civilian Satellites, *Journal of Remote Sensing*, *2022*, doi:10.34133/2022/9769536.

Chulakadabba, A., et al. (2023), Methane point source quantification using MethaneAIR: a new airborne imaging spectrometer, *Atmospheric Measurement Techniques*, *16*(23), 5771-5785, doi:10.5194/amt-16-5771-2023.

Cusworth, D. H., et al. (2021), Intermittency of Large Methane Emitters in the Permian Basin, *Environmental Science & Technology Letters*, *8*(7), 567-573, doi:10.1021/acs.estlett.1c00173.

Cusworth, D. H., et al. (2019), Potential of next-generation imaging spectrometers to detect and quantify methane point sources from space, *Atmospheric Measurement Techniques*, *12*(10), 5655-5668, doi:10.5194/amt-12-5655-2019.

Cusworth, D. H., et al. (2022), Strong methane point sources contribute a disproportionate fraction of total emissions across multiple basins in the United States, *Proceedings of the National Academy of Sciences*, *119*(38), e2202338119, doi:10.1073/pnas.2202338119.

Dennison, P. E., A. K. Thorpe, D. A. Roberts, and R. O. Green (2013), Modeling sensitivity of imaging spectrometer data to carbon dioxide and methane plumes, paper presented at 2013 5th Workshop on Hyperspectral Image and Signal Processing: Evolution in Remote Sensing (WHISPERS), 26-28 June 2013.

Duren, R. M., et al. (2019), California's methane super-emitters, *Nature*, *575*(7781), 180-184, doi:10.1038/s41586-019-1720-3.

Ehret, T., A. De Truchis, M. Mazzolini, J.-M. Morel, A. d'Aspremont, T. Lauvaux, R. Duren, D. Cusworth, and G. Facciolo (2022), Global Tracking and Quantification of Oil and Gas Methane Emissions from Recurrent Sentinel-2 Imagery, *Environmental Science & Technology*, *56*(14), 10517-10529, doi:10.1021/acs.est.1c08575.

Eismann, M. (2012), Hyperspectral Remote Sensing (SPIE Press Book), edited, SPIE press book.

Esparza, Á. E., G. Rowan, A. Newhook, H. J. Deglint, B. Garrison, B. Orth-Lashley, M. Girard, and W. Shaw (2023), Analysis of a tiered top-down approach using satellite and aircraft platforms to monitor oil and gas facilities in the Permian basin, *Renewable and Sustainable Energy Reviews*, *178*, 113265, doi:10.1016/j.rser.2023.113265.

Federal Reserve Bank of Dallas (FRBD): Energy in the Eleventh District: Permian Basin: Oil production, https://www.dallasfed.org/research/energy11/permian.aspx#Oil, last access: 12 October 2022.

Foote, M. D., P. E. Dennison, A. K. Thorpe, D. R. Thompson, S. Jongaramrungruang, C. Frankenberg, and S. C. Joshi (2020), Fast and Accurate Retrieval of Methane Concentration From Imaging Spectrometer Data Using Sparsity Prior, *IEEE Transactions on Geoscience and Remote Sensing*, *58*(9), 6480-6492, doi:10.1109/TGRS.2020.2976888.

Frankenberg, C., J. F. Meirink, M. van Weele, U. Platt, and T. Wagner (2005), Assessing Methane Emissions from Global Space-Borne Observations, *Science*, *308*(5724), 1010-1014, doi:10.1126/science.1106644.

Frankenberg, C., et al. (2016), Airborne methane remote measurements reveal heavy-tail flux distribution in Four Corners region, *Proceedings of the National Academy of Sciences*, *113*(35), 9734-9739, doi:10.1073/pnas.1605617113.

Gordon, I. E., et al. (2017), The HITRAN2016 molecular spectroscopic database, *Journal of Quantitative Spectroscopy and Radiative Transfer*, *203*, 3-69, doi:10.1016/j.jqsrt.2017.06.038.

Guanter, L., I. Irakulis-Loitxate, J. Gorroño, E. Sánchez-García, D. H. Cusworth, D. J. Varon, S. Cogliati, and R. Colombo (2021), Mapping methane point emissions with the PRISMA spaceborne imaging spectrometer, *Remote Sensing of Environment*, *265*, 112671, doi:10.1016/j.rse.2021.112671.

International Energy Agency. Methane tracker 2020 [Online]. Available: https://www.iea.org/reports/methane-tracker-2020; 2020.

Irakulis-Loitxate, I., J. Gorroño, D. Zavala-Araiza, and L. Guanter (2022a), Satellites Detect a Methane Ultra-emission Event from an Offshore Platform in the Gulf of Mexico, *Environmental Science & Technology Letters*, *9*(6), 520-525, doi:10.1021/acs.estlett.2c00225.

Irakulis-Loitxate, I., et al. (2021), Satellite-based survey of extreme methane emissions in the Permian basin, *Science Advances*, *7*(27), eabf4507, doi:10.1126/sciadv.abf4507.

Irakulis-Loitxate, I., L. Guanter, J. D. Maasakkers, D. Zavala-Araiza, and I. Aben (2022b), Satellites Detect Abatable Super-Emissions in One of the World's Largest Methane Hotspot Regions, *Environmental Science & Technology*, *56*(4), 2143-2152, doi:10.1021/acs.est.1c04873.

Jacob, D. J., A. J. Turner, J. D. Maasakkers, J. Sheng, K. Sun, X. Liu, K. Chance, I. Aben, J. McKeever, and C. Frankenberg (2016), Satellite observations of atmospheric methane and their value for quantifying methane emissions, *Atmospheric Chemistry and Physics*, *16*(22), 14371-14396, doi:10.5194/acp-16-14371-2016.

Jacob, D. J., et al. (2022), Quantifying methane emissions from the global scale down to point sources using satellite observations of atmospheric methane, *Atmospheric Chemistry and Physics*, *22*(14), 9617-9646, doi:10.5194/acp-22-9617-2022.

Jervis, D., J. McKeever, B. O. A. Durak, J. J. Sloan, D. Gains, D. J. Varon, A. Ramier, M. Strupler, and E. Tarrant (2021), The GHGSat-D imaging spectrometer, *Atmospheric Measurement Techniques*, *14*(3), 2127-2140, doi:10.5194/amt-14-2127-2021.

Liu, Y. N., et al. (2019), The Advanced Hyperspectral Imager: Aboard China's GaoFen-5 Satellite, *IEEE Geoscience and Remote Sensing Magazine*, *7*(4), 23-32, doi:10.1109/MGRS.2019.2927687.

Li, F., et al. (2023). Mapping methane super-emitters in China and United States with GF5-02 hyperspectral imaging spectrometer[J]. *National Remote Sensing Bulletin*, 2023 (null): 1-15, doi: 10.11834/jrs.20232453.

Lu, X., et al. (2023), Observation-derived 2010-2019 trends in methane emissions and intensities from US oil and gas fields tied to activity metrics, *Proceedings of the National Academy of Sciences*, *120*(17), e2217900120, doi:10.1073/pnas.2217900120.

Lyon, D. R., R. A. Alvarez, D. Zavala-Araiza, A. R. Brandt, R. B. Jackson, and S. P. Hamburg (2016), Aerial Surveys of Elevated Hydrocarbon Emissions from Oil and Gas Production Sites, *Environmental Science & Technology*, *50*(9), 4877-4886, doi:10.1021/acs.est.6b00705.

Lyon, D. R., et al. (2021), Concurrent variation in oil and gas methane emissions and oil price during the COVID-19 pandemic, *Atmospheric Chemistry and Physics*, *21*(9), 6605-6626, doi:10.5194/acp-21-6605-2021.

Maasakkers, J. D., et al. (2023), A Gridded Inventory of Annual 2012–2018 U.S. Anthropogenic Methane Emissions, *Environmental Science & Technology*, *57*(43), 16276-16288, doi:10.1021/acs.est.3c05138.

Mayfield, E. N., A. L. Robinson, and J. L. Cohon (2017), System-wide and Superemitter Policy Options for the Abatement of Methane Emissions from the U.S. Natural Gas System, *Environmental Science & Technology*, *51*(9), 4772-4780, doi:10.1021/acs.est.6b05052.

Pandey, S., M. van Nistelrooij, J. D. Maasakkers, P. Sutar, S. Houweling, D. J. Varon, P. Tol, D. Gains, J. Worden, and I. Aben (2023), Daily detection and quantification of methane leaks using Sentinel-3: a tiered satellite observation approach with Sentinel-2 and Sentinel-5p, *Remote Sensing of Environment*, *296*, 113716, doi:10.1016/j.rse.2023.113716.

Roger, J., I. Irakulis-Loitxate, A. Valverde, J. Gorroño, S. Chabrillat, M. Brell, and L. Guanter (2024), High-resolution methane mapping with the EnMAP satellite imaging spectroscopy mission, *IEEE Transactions on Geoscience and Remote Sensing*, 1-1, doi:10.1109/TGRS.2024.3352403.

Rutherford, J. S., E. D. Sherwin, A. P. Ravikumar, G. A. Heath, J. Englander, D. Cooley, D. Lyon, M. Omara, Q. Langfitt, and A. R. Brandt (2021), Closing the methane gap in US oil and natural gas production emissions inventories, *Nature Communications*, *12*(1), 4715, doi:10.1038/s41467-021-25017-4.

Scarpelli, T. R., D. J. Jacob, S. Grossman, X. Lu, Z. Qu, M. P. Sulprizio, Y. Zhang, F. Reuland, D. Gordon, and J. R. Worden (2022), Updated Global Fuel Exploitation Inventory (GFEI) for methane emissions from the oil, gas, and coal sectors: evaluation with inversions of atmospheric methane observations, *Atmospheric Chemistry and Physics*, *22*(5), 3235-3249, doi:10.5194/acp-22-3235-2022.

Shen, L., et al. (2022), Satellite quantification of oil and natural gas methane emissions in the US and Canada including contributions from individual basins, *Atmospheric Chemistry and Physics*, *22*(17), 11203-11215, doi:10.5194/acp-22-11203-2022.

Szeliski, R. (2022), Computer vision: algorithms and applications, Springer Nature.

Sherwin, E., S. El Abbadi, P. Burdeau, Z. Zhang, Z. Chen, J. Rutherford, Y. Chen, and A. Brandt (2023a), Single-blind test of nine methane-sensing satellite systems from three continents, *EarthArXiv eprints*, X56089.

Sherwin, E. D., J. S. Rutherford, Y. Chen, S. Aminfard, E. A. Kort, R. B. Jackson, and A. R. Brandt (2023b), Single-blind validation of space-based point-source detection and quantification of onshore methane emissions, *Scientific Reports*, *13*(1), 3836, doi:10.1038/s41598-023-30761-2.

Thompson, D. R., et al. (2015), Real-time remote detection and measurement for airborne imaging spectroscopy: a case study with methane, *Atmospheric Measurement Techniques*, *8*(10), 4383-4397, doi:10.5194/amt-8-4383-2015.

Thompson, D. R., A. K. Thorpe, C. Frankenberg, R. O. Green, R. Duren, L. Guanter, A. Hollstein, E. Middleton, L. Ong, and S. Ungar (2016), Space-based remote imaging spectroscopy of the Aliso Canyon CH4 superemitter, *Geophysical Research Letters*, *43*(12), 6571-6578, doi:10.1002/2016GL069079.

Thorpe, A. K., et al. (2016), Mapping methane concentrations from a controlled release experiment using the next generation airborne visible/infrared imaging spectrometer (AVIRIS-NG), *Remote Sensing of Environment*, *179*, 104-115, doi:10.1016/j.rse.2016.03.032.

Thorpe, A. K., et al. (2023a), Attribution of individual methane and carbon dioxide emission sources using EMIT observations from space, *Science Advances*, *9*(46), eadh2391, doi:10.1126/sciadv.adh2391.

Thorpe, A. K., et al. (2023b), Methane emissions decline from reduced oil, natural gas, and refinery production during COVID-19, *Environmental Research Communications*, *5*(2), 021006, doi:10.1088/2515-7620/acb5e5.

Thorpe, A. K., et al. (2021), Improved methane emission estimates using AVIRIS-NG and an Airborne Doppler Wind Lidar, *Remote Sensing of Environment*, *266*, 112681, doi:10.1016/j.rse.2021.112681.

Tollefson, J. (2022), Scientists raise alarm over 'dangerously fast' growth in atmospheric methane, *Nature*, doi:10.1038/d41586-022-00312-2.

Varon, D. J., D. J. Jacob, J. McKeever, D. Jervis, B. O. A. Durak, Y. Xia, and Y. Huang (2018), Quantifying methane point sources from fine-scale satellite observations of atmospheric methane plumes, *Atmospheric Measurement Techniques*, *11*(10), 5673-5686, doi:10.5194/amt-11-5673-2018.

Varon, D. J., D. Jervis, J. McKeever, I. Spence, D. Gains, and D. J. Jacob (2021), High-frequency monitoring of anomalous methane point sources with multispectral Sentinel-2 satellite observations, *Atmospheric Measurement Techniques*, *14*(4), 2771-2785, doi:10.5194/amt-14-2771-2021.

Vaughn, T. L., C. S. Bell, C. K. Pickering, S. Schwietzke, G. A. Heath, G. Pétron, D. J. Zimmerle, R. C. Schnell, and D. Nummedal (2018), Temporal variability largely explains top-down/bottom-up difference in methane emission estimates from a natural gas production region, *Proceedings of the National Academy of Sciences*, *115*(46), 11712-11717, doi:10.1073/pnas.1805687115.

Yu, J., B. Hmiel, D. R. Lyon, J. Warren, D. H. Cusworth, R. M. Duren, Y. Chen, E. C. Murphy, and A. R. Brandt (2022), Methane Emissions from Natural Gas Gathering Pipelines in the Permian Basin, *Environmental Science & Technology Letters*, *9*(11), 969-974, doi:10.1021/acs.estlett.2c00380.

Zavala-Araiza, D., et al. (2021), A tale of two regions: methane emissions from oil and gas production in offshore/onshore Mexico, *Environmental Research Letters*, *16*(2), 024019, doi:10.1088/1748-9326/abceeb.

Figure 1. Sensitivity of GF5-01A/02-AHSI shortwave infrared (SWIR) measurements to methane. (a) Example of a unit methane absorption spectrum *k* used as target signature by the matched filter retrieval method used in this study. (b) Simulated top-of-atmosphere radiance spectra in the SWIR as measured by GF5-01A/02-AHSI. (c) Two-way transmittance of greenhouse gases with the highest absorption in the SWIR part of the spectrum.

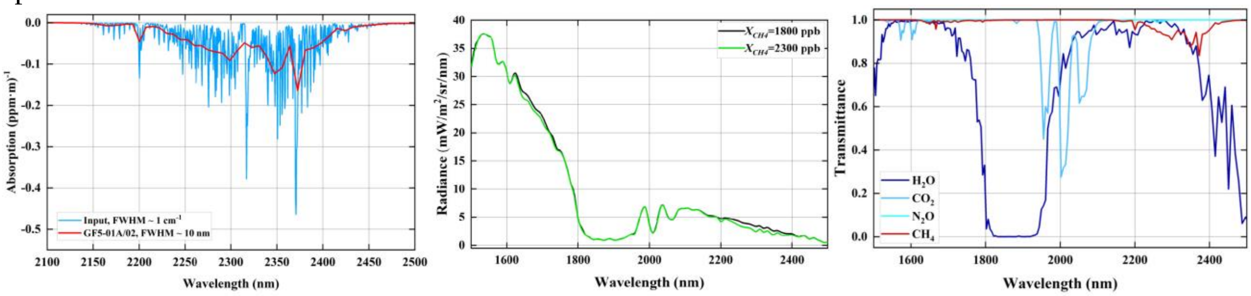

(a) Unit methane absorption spectrum **(b) Sensitivity to CH_4 enhancements** **(c) Two-way transmittance of greenhouse gases**

Figure 2. Major basins surveyed between 2022 and 2023 with the spaceborne imaging spectrometers. Subpanels show the location and intensity of the detected methane point source emissions.

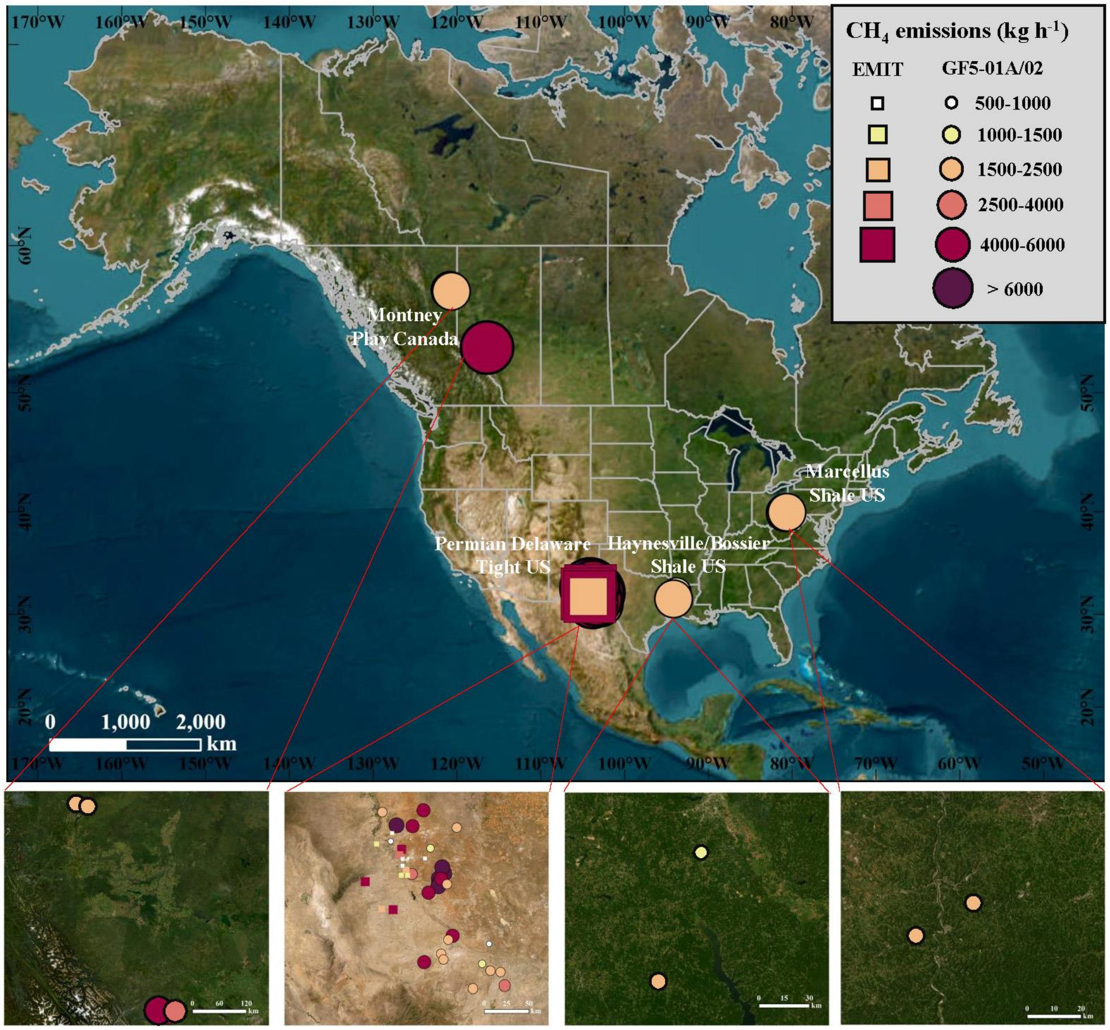

Figure 3. The representative methane plumes from various emission sources in North America, including tank battery, compressor station, flaring and wellhead.

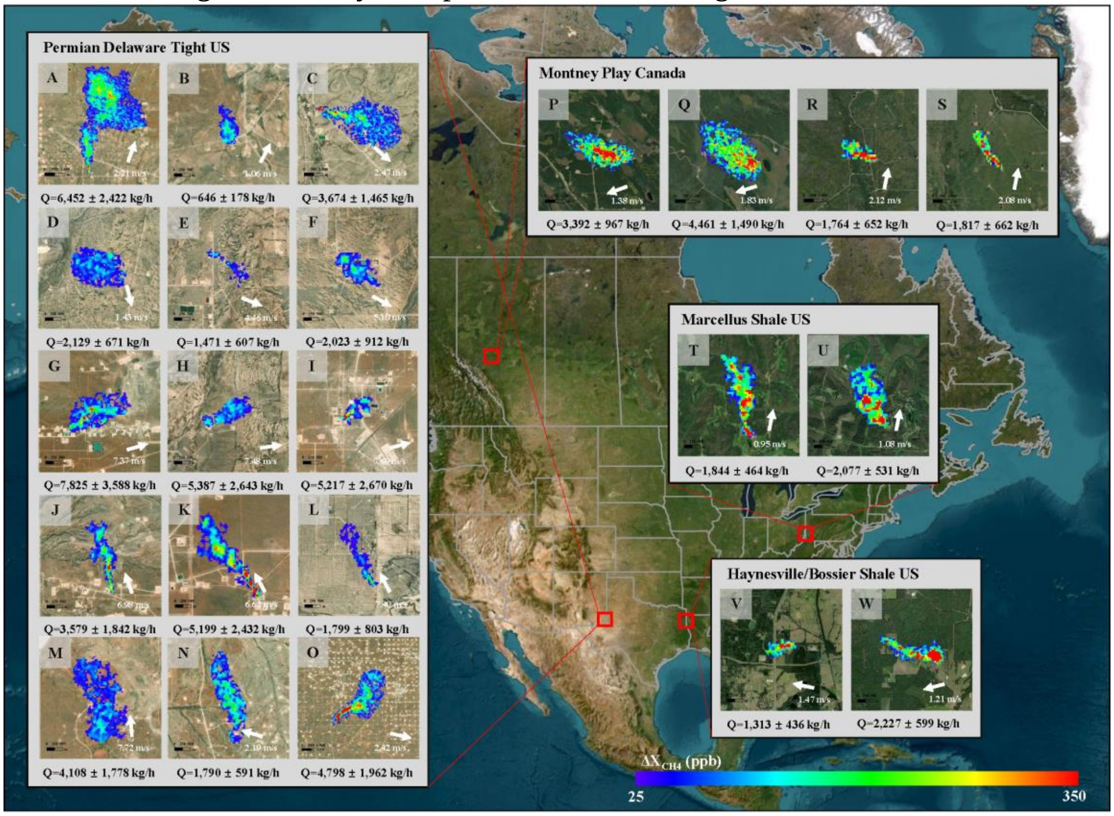

Figure 4. Relative frequency for the 48 methane plumes detected over North America with satellite imaging spectroscopy. The inset bar shows a comparison of methane point source emissions. Vertical error bars correspond to 1-σ precision errors in in flux rate calculation.

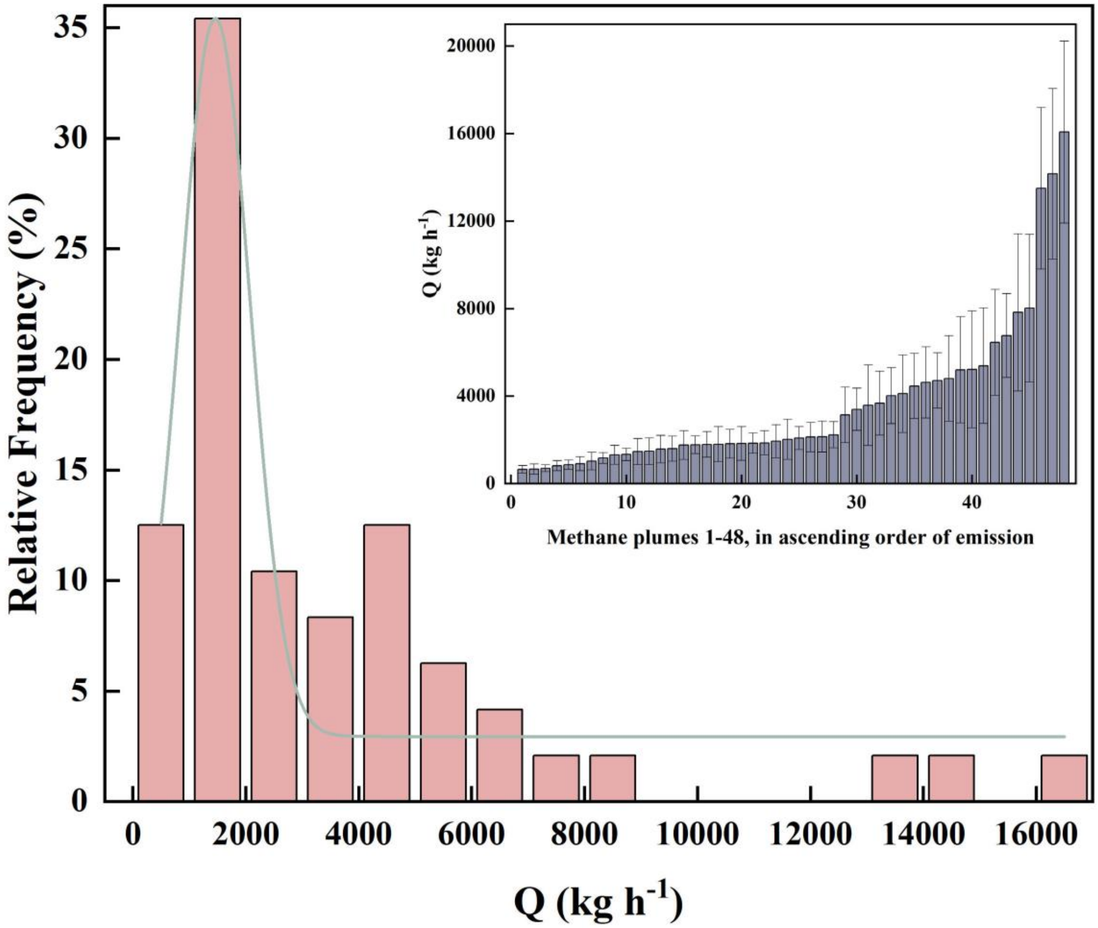

Figure 5. Comparison of emission estimates of methane plumes between surveys. The surveys for the multiple basins in the US are selected as the references. They report 5593 and 37 methane plumes, while our survey attempts 48 plumes. Violin plots show statistical distributions of methane plume emission rates for these surveys. For each survey, the black dot represents the median value. The shading represents the number distribution of the methane plumes with different emission rates.

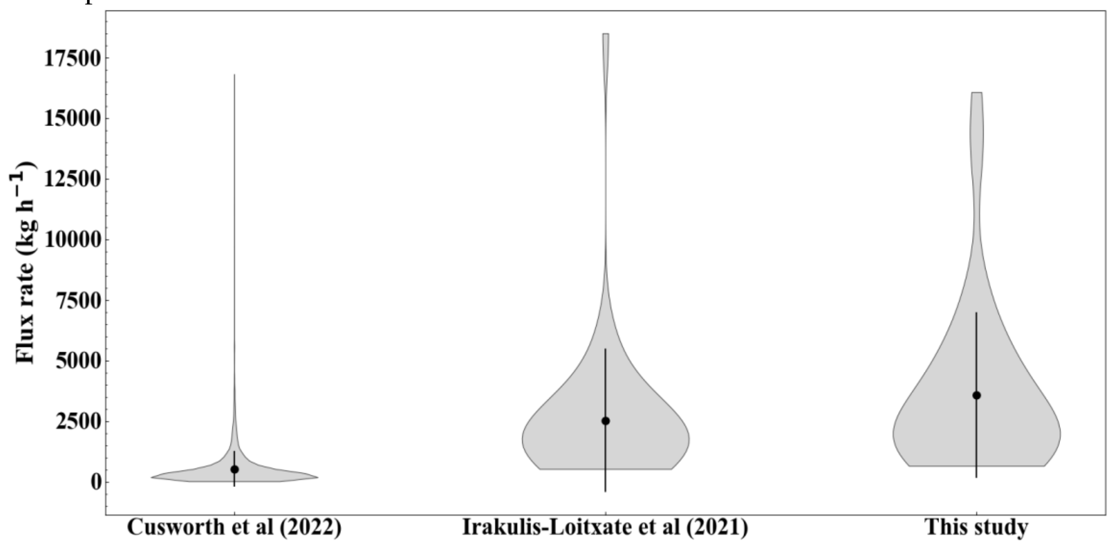

Figure 6. The cumulative distribution of methane point-source emissions quantified for each survey. Data for Permian 2019-2020 and multiple basins 2019-2021 in the US come from Irakulis-Loitxate *et al* (2021) and Cusworth *et al* (2022) respectively.

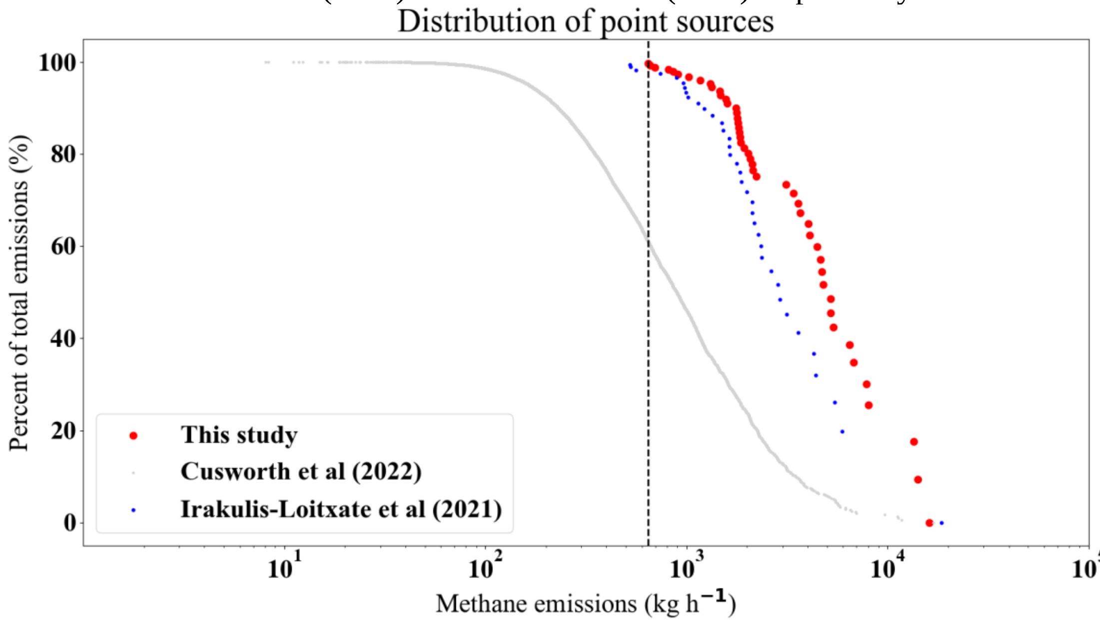

Figure 7. Summary statistics for each basin surveyed between 2022 and 2023. Comparison between aggregated point-source emissions for each survey with a top-down flux inversion with GOSAT/TROPOMI observations and bottom-up emission from the updated global fuel exploitation inventory (GFEI v2).

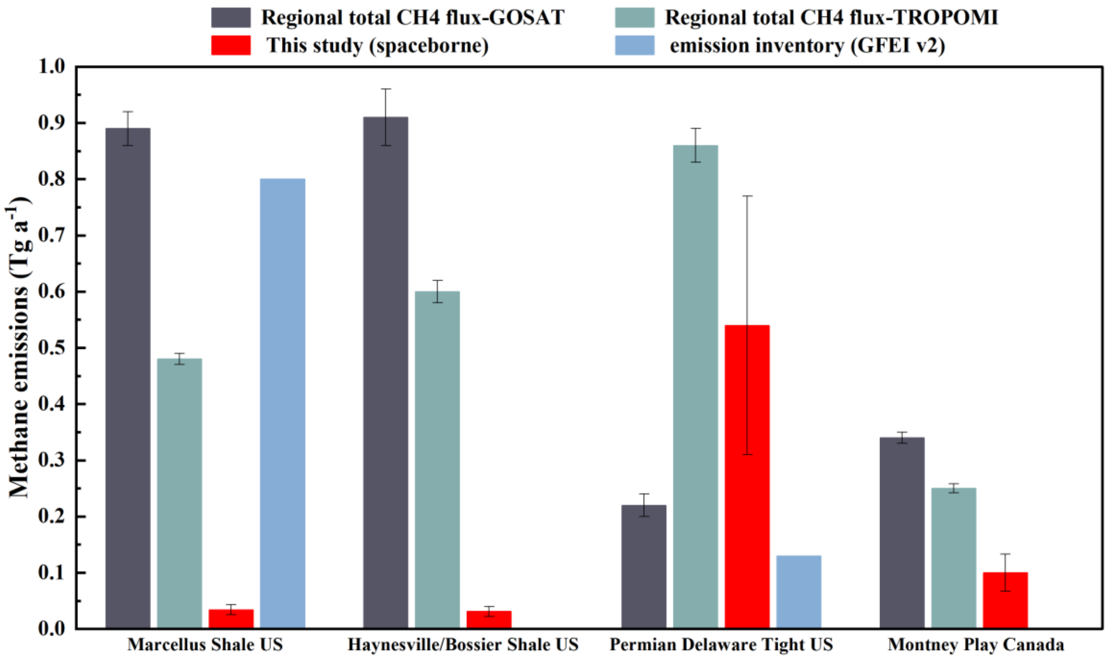

Figure 8. Comparison of regional methane enhancement (a), TROPOMI-based flux inversions (b), Kriging interpolation-based flux inversions (c) and bottom-up inventory (EPA greenhouse gas inventory) (d) for Permian Delaware Tight US.

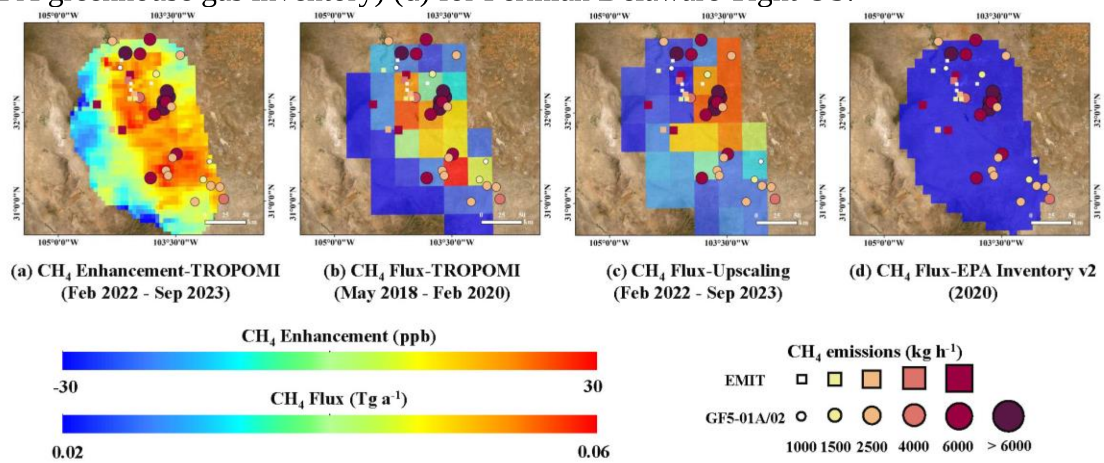

Figure 9. Distribution of methane emissions for multiple basins over the North America with spaceborne/airborne imaging spectroscopy. (a) Multi-month spaceborne surveys in North America. (b) Comparisons of airborne/spaceborne surveys in Permian Delaware Tight US before and after COVID-19.

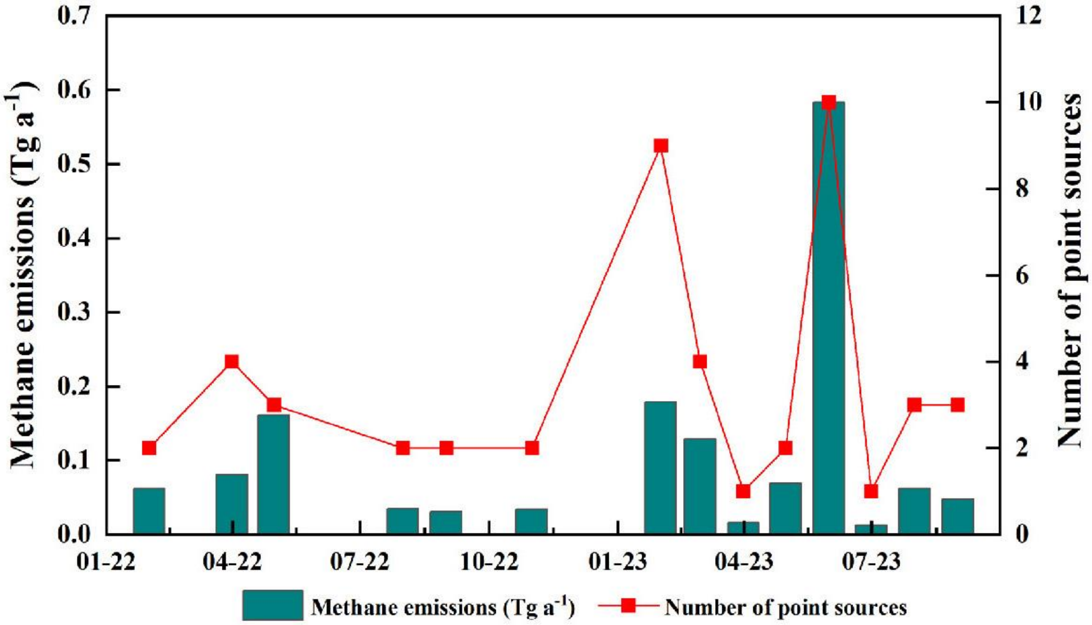

(a) Multi-month spaceborne surveys in North America

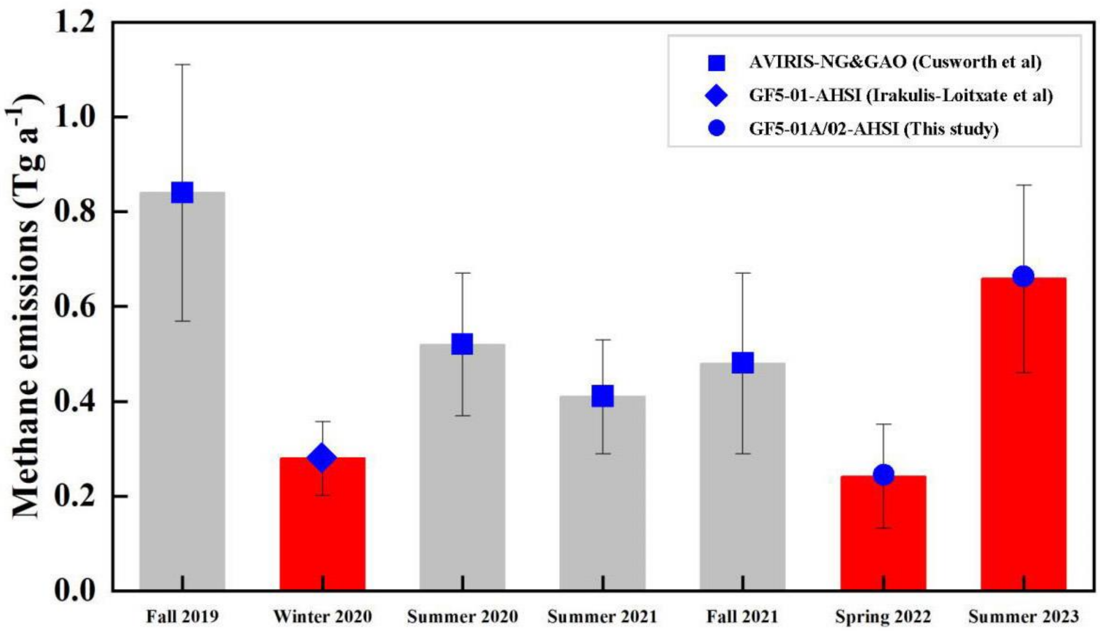

(b) Comparisons of airborne/spaceborne surveys in Permian Delaware Tight US

Figure 10. Breakdown of spaceborne/airborne-detected methane emissions in North America. Emissions are classified in terms of the emission source (a) and of the emission sector (b).

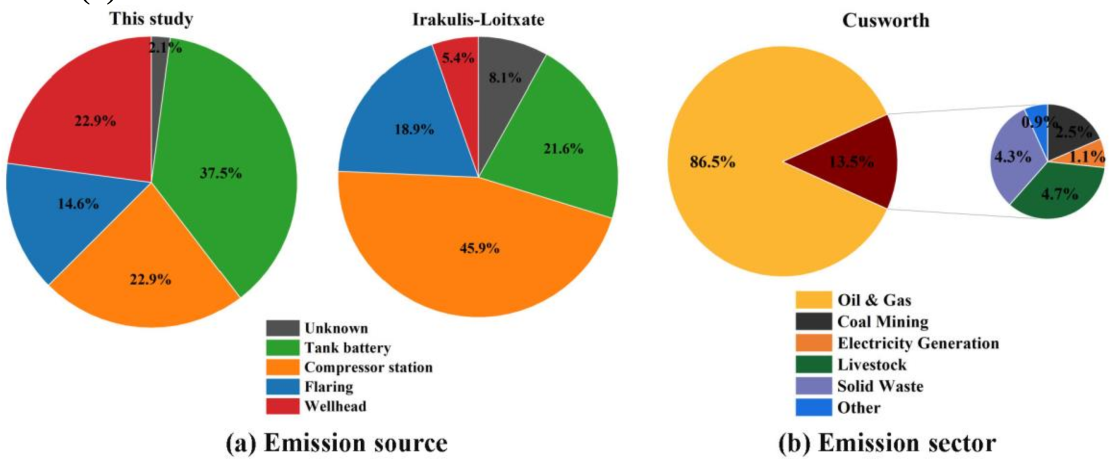

Table 1. Satellite instruments for mapping methane point-source emissions used in this study.

Mission	Spatial resolution	Spectral resolution	Spatial coverage	Temporal resolution	Period of operation
GF5-01A	30 m×30 m	10 nm	60 km×60 km	51 days	Dec.2022 - present
GF5-02	30 m×30 m	10 nm	60 km×60 km	51 days	Sep.2021 - present
EMIT	60 m×60 m	7.4 nm	80 km×80 km	36.5 days	Jul.2022 - present

Table 2. The list of bottom-up emission inventory and top-down emission estimate.

Data	Mission	Spatial resolution	Time	Data sources
Bottom-up emission inventory	GFEI v2	0.1°×0.1°	2019	HARVARD Dataverse (https://doi.org/10.7910/DVN/HH4EUM)
	EPA v2	0.1°×0.1°	2020	United States Environmental Protection Agency (https://www.epa.gov/ghgemissions/us-gridded-methane-emissions)
Top-down emission estimate	TROPOMI	0.25°×0.3125°	05/2018 ~02/2020	Peking University Open Research Data (https://doi.org/10.18170/DVN/JPKFU6)
	GOSAT	0.5°×0.625°	2019	GitHub (https://github.com/luxiaoatchemsysu/Data-USoilgasCH4)